

## Article

# The Heterostructures of CuO and SnO<sub>x</sub> for NO<sub>2</sub> Detection

Anna Paleczek <sup>1</sup>, Bartłomiej Szafraniak <sup>1</sup>, Łukasz Fuśnik <sup>1,\*</sup>, Andrzej Brudnik <sup>1</sup>, Dominik Grochala <sup>1</sup>,  
Stanisława Kluska <sup>2</sup>, Maria Jurzecka-Szymacha <sup>2</sup>, Erwin Maciak <sup>3</sup>, Piotr Kałużyński <sup>3</sup> and Artur Rydosz <sup>1</sup>

- <sup>1</sup> Faculty of Computer Science, Electronics and Telecommunications, AGH University of Science and Technology, al. A. Mickiewicza 30, 30-059 Krakow, Poland; anna.paleczek@op.pl (A.P.); szafrani@agh.edu.pl (B.S.); brudnik@agh.edu.pl (A.B.); grochala@agh.edu.pl (D.G.); rydosz@agh.edu.pl (A.R.)
- <sup>2</sup> Faculty of Materials Science and Ceramics, AGH University of Science and Technology, al. A. Mickiewicza 30, 30-059 Kraków, Poland; kluska@agh.edu.pl (S.K.); maria@agh.edu.pl (M.J.-S.)
- <sup>3</sup> Department of Optoelectronics, Silesian University of Technology, 2 Krzywoustego Str., 44-100 Gliwice, Poland; erwin.maciak@polsl.pl (E.M.); piotr.kaluzynski@polsl.pl (P.K.)
- \* Correspondence: lfusnik@agh.edu.pl; Tel.: +48-126-172-900

**Abstract:** Controlling environmental pollution is a burning problem for all countries more than ever. Currently, due to the increasing industrialization, the number of days when the limits of air pollutants are over the threshold levels exceeds 80–85% of the year. Therefore, cheap and effective sensors are always welcome. One idea is to combine such solutions with cars and provide real-time information about the current pollution level. However, the environmental conditions are demanding, and thus the developed sensors need to be characterized by the high 3S parameters: sensitivity, stability and selectivity. In this paper, we present the results on the heterostructure of CuO/SnO<sub>x</sub> and SnO<sub>x</sub>/CuO as a possible approach for selective NO<sub>2</sub> detection. The developed gas sensors exhibited lower operating temperature and high response in the wide range of NO<sub>2</sub> and in a wide range of relative humidity changes. Material characterizations and impedance spectroscopy measurements were also conducted to analyze the chemical and electrical behavior.

**Keywords:** copper oxide; CuO; gas-sensing; impedance spectroscopy; NO<sub>2</sub> detection; SnO<sub>x</sub>; tin oxide



**Citation:** Paleczek, A.; Szafraniak, B.; Fuśnik, Ł.; Brudnik, A.; Grochala, D.; Kluska, S.; Jurzecka-Szymacha, M.; Maciak, E.; Kałużyński, P.; Rydosz, A. The Heterostructures of CuO and SnO<sub>x</sub> for NO<sub>2</sub> Detection. *Sensors* **2021**, *21*, 4387. <https://doi.org/10.3390/s21134387>

Academic Editor:  
Gagaoudakis Emmanouil

Received: 17 May 2021  
Accepted: 23 June 2021  
Published: 26 June 2021

**Publisher's Note:** MDPI stays neutral with regard to jurisdictional claims in published maps and institutional affiliations.



**Copyright:** © 2021 by the authors. Licensee MDPI, Basel, Switzerland. This article is an open access article distributed under the terms and conditions of the Creative Commons Attribution (CC BY) license (<https://creativecommons.org/licenses/by/4.0/>).

## 1. Introduction

With the development of industry, technology and environmental awareness, the need to monitor emissions and levels of gases in the atmosphere increases. According to market research, the gas sensor market will develop dynamically [1–3]. One of the main gases with a negative impact on the environment and human health is nitrogen dioxide (NO<sub>2</sub>). According to the guidelines of the World Health Organization (WHO) [4], the current guideline values of 40 µg/m<sup>3</sup>, which corresponds to 21.3 ppb (annual average), and 100 µg/m<sup>3</sup> (1 h average), which corresponds to 106.4 ppb, have negative effects on health. NO<sub>2</sub>, considered as an air pollutant, has several interrelated activities. Even at short-term concentrations above 200 µg/m<sup>3</sup>, it is a toxic gas causing inflammation in the respiratory tract [4]. NO<sub>2</sub> is a source of nitrate aerosols, an important fraction of PM<sub>2.5</sub>, and in the presence of ozone ultraviolet light. The sources of anthropogenic NO<sub>2</sub> emissions include combustion processes (heating, energy production, engines in vehicles and ships). Epidemiological studies have shown that prolonged exposure of children with asthma to NO<sub>2</sub> exacerbates the symptoms of bronchitis [5]. The WHO Guidelines for Indoor Air Quality [4] provides a detailed and concise summary of studies on the effects of nitrogen oxides on human health. Moreover, a correlation was observed between the decrease in lung function and the increase in NO<sub>2</sub> concentrations currently measured in the cities of Europe and North America [5]. The European Union also referred to the guideline values set by WHO in [6]. Different countries have nonidentical permissible levels of NO<sub>2</sub>. Various acceptable levels resulting from miscellaneous regulations and standards are not wide and therefore significant. An example of the permissible NO<sub>2</sub> concentrations in the

United States of America are presented in [7]. Currently, in accordance with the European Union Euro 6 standard, the permissible levels of pollutant emissions from cars, including  $\text{NO}_2$ , have been significantly reduced; for example,  $\text{NO}_x$  emissions should not exceed 0.08 g/km [8–10]. Increasingly higher standards and requirements for exhaust emissions from means of transport require more and more accurate gas sensors necessary to control exhaust emissions. There is now more and more research on this subject. One of the many examples of car tests for exhaust emissions, especially  $\text{NO}_x$ , is found in [11].

Many types of gas sensors are used to detect the presence of  $\text{NO}_2$  [12], including electrochemical sensors [13], catalytic sensors, optical sensors—infrared absorption (Infra-Red) and semiconductor sensors, which are also used in mass resonant [14–18]. Various materials are used in the production of semiconductor gas sensors, such as  $\text{MoS}_2$  [19]. Carbon based materials, such as carbon nanotubes (CNTs) [20] and graphene oxide [21], are also used for gas detection. Currently, the most popular resistance sensors are metal oxide semiconductor sensors (MOX) [13,22–30]. Various metal oxides are used as gas sensors; for example, barium titanate, strontium titanate and barium strontium titanate doped with various elements depending on the doped materials; they behave as p-type or n-type [31,32], n-type including zinc oxide ( $\text{ZnO}$ ) [33,34], tin dioxide ( $\text{SnO}_2$ ) [35], tungsten trioxide ( $\text{WO}_3$ ) [36], indium oxide ( $\text{In}_2\text{O}_3$ ), gallium oxide ( $\text{Ga}_2\text{O}_3$ ), vanadium oxide ( $\text{V}_2\text{O}_5$ ) and iron oxide ( $\text{Fe}_2\text{O}_3$ ) and p-type metal oxides such as nickel oxide ( $\text{NiO}$ ), copper oxide ( $\text{CuO}$ ) [37], cobalt oxide ( $\text{Co}_3\text{O}_4$ ), manganese oxide ( $\text{Mn}_3\text{O}_4$ ) and chromium oxide ( $\text{Cr}_2\text{O}_3$ ) [38,39]. As gas-sensitive materials in gas sensors, heterostructures are also used, such as tin sulfide/tin oxide ( $\text{SnS}_2/\text{SnO}_2$ ), tungsten disulfide/titanium dioxide ( $\text{WS}_2/\text{TiO}_2$ ), molybdenum disulfide/tin oxide ( $\text{MoS}_2/\text{SnO}_2$ ), molybdenum disulfide/zinc oxide ( $\text{MoS}_2/\text{ZnO}$ ), reduced graphene oxide/tin oxide ( $\text{rGO}/\text{SnO}_2$ ), reduced graphene oxide/carbon dot ( $\text{rGO}/\text{CD}$ ), reduced graphene oxide/molybdenum disulfide ( $\text{rGO}/\text{MoS}_2$ ) [40], reduced graphene oxide/iron oxide ( $\text{rGO}/\text{Fe}_2\text{O}_3$ ) [41], cobalt tetroxide/titanium dioxide ( $\text{Co}_3\text{O}_4/\text{TiO}_2$ ) [42], zinc oxide/indium oxide ( $\text{ZnO}/\text{In}_2\text{O}_3$ ), tin oxide/cupric oxide ( $\text{SnO}_2/\text{CuO}$ ), titanium dioxide/vanadium pentoxide ( $\text{TiO}_2/\text{V}_2\text{O}_5$ ) [30], graphene in combination with metal oxides [43] and many others.

In this paper, the gas sensors based on the heterostructures of tin oxide and copper oxide were investigated for  $\text{NO}_2$  detection in a wide range of concentrations. The deposited films exhibited very good selectivity to VOCs such as ethanol and acetone, and thanks to heterostructures of n-type/p-type and p-type/n-type, the influence of relative humidity was compensated. Additionally, measurements were made by impedance spectroscopy in order to determine the parameters of the equivalent electrical model for the tested nanomaterials.

## 2. Materials and Methods

### 2.1. Gas Sensor Substrates

As gas sensor substrates, a commercially available CC2 BVT alumina-based sensor substrate with electrodes were used (Figure 1a,b). After the cleaning process in an ultrasonic bath, the gas sensor substrates were placed in the deposition chamber and gas-sensitive layers were deposited as described in the sections below and schematically presented in Figure 1c.

### 2.2. Gas-Sensitive Layer Deposition

The gas-sensitive layers were obtained in the commercially available magnetron sputtering deposition system from Kurt J. Lesker Company (Hastings, East Sussex, UK), in details presented and discussed [44]. Briefly, the Ultra High Vacuum multitarget deposition system was equipped with the EpiCentre Right-angle (ECR) manipulator, which enables the deposition with the utilization of the glancing angle deposition (GLAD) technique, where deposition angle, rotation and deposition temperature are crucial parameters and can be changed by changing the ECR manipulator properties (Figure 1c). Thanks to the multitarget feature, copper and tin metal targets were used during the deposition in

reaction mode without changing the deposition conditions. Such realization enables the deposition of heterostructures without any interlayer between both semiconductors.

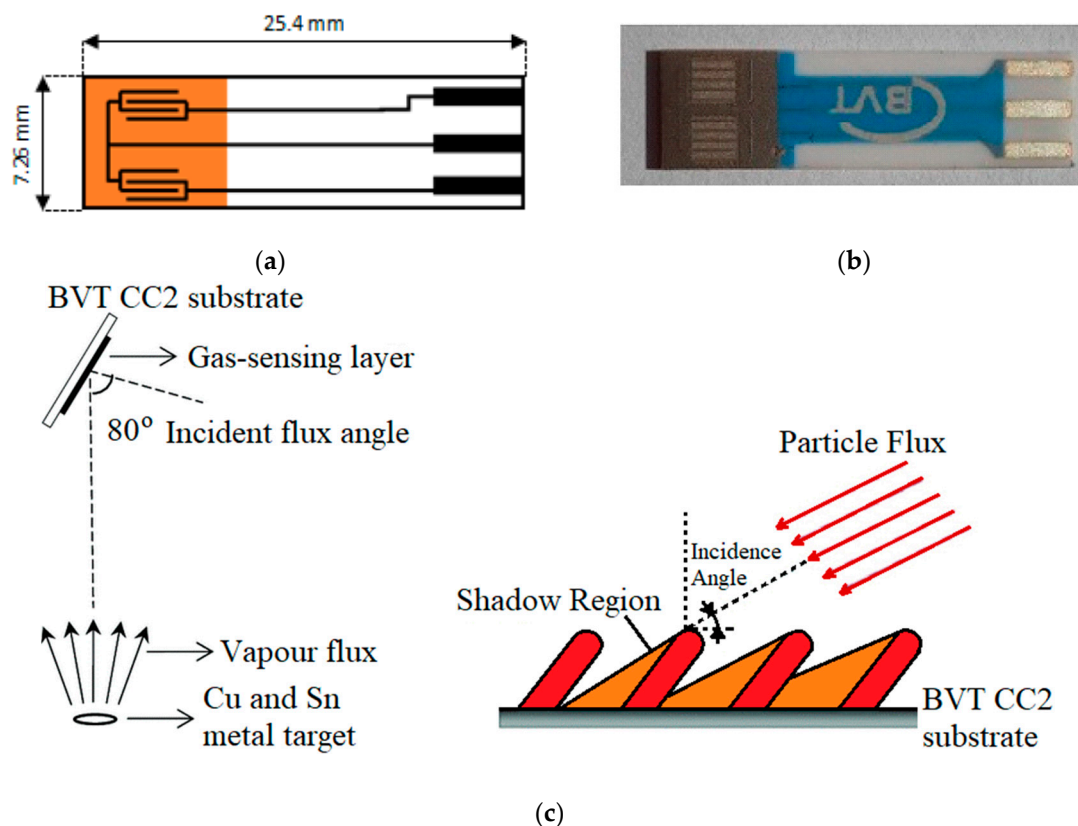


**Figure 1.** (a) Scheme and (b) picture of the CC2 BVT gas sensor substrate with deposited gas-sensing films; (c) the sketch of the theoretical deposition of nanostructures due to the glancing angle deposition (GLAD). Reprinted with permission from ref. [37] under CC B.Y. 4.0.

### 2.2.1. Tin Oxide

The tin oxide thin films were deposited in DC MF (direct current medium frequency) mode from Sn metallic target (purity 4 N—99.99%) by applying reactive sputtering under a mixture of 34% argon and 66% oxygen (purity of gases 5 N—99.999%). The deposition process parameters have been kept as in the previously reported paper, where single tin oxide-based gas-sensing layers were deposited [35,45]. In brief, the base vacuum and deposition vacuum were  $1 \times 10^{-5}$  mbar and  $2 \times 10^{-2}$  mbar, respectively. The deposition temperature was set to 200 °C and deposition time was adjusted to deposit various thicknesses with a constant power of 50 W [35,45].

### 2.2.2. Copper Oxide

The copper oxide thin films were deposited in the same DC MF (direct current medium frequency) mode as tin oxide (Cu target purity 4 N—99.99%), and under the same pressure and gas-mixture condition (purity of gases 5 N—99.999%), which are different in comparison with those previously reported [37,46]. However, thanks to the previous experiments with Emission Optical Spectroscopy [47], the reactive atmosphere can be controlled to provide stable and repeatable conditions.

### 2.3. Gas-Sensing Measurements

Measurements of the sensor properties of the prepared samples were performed on a dedicated setup, consisting of a measuring chamber with a volume of about 300 cm<sup>3</sup>, with the possibility of regulating and stabilizing the temperature of the sensor in the

chamber (previously presented in [48]). The target gases were supplied to the chamber via MFC controllers from gas canisters (Air Liquid, Cracow, Poland) with various initial concentrations ranging from 0.5–20 ppm. The measurement of changes in the resistance of the gas sensor was carried out using a Keithley 6517 electrometer operating with a constant test voltage of 1V. The measuring station also enables the measurement of frequency characteristics using the Solartron ModuLab XM MTS system. The measurement data were collected via a dedicated software.

### 2.3.1. Measurements of Resistance Changes with Direct Current (DC)

Each sample underwent the same measurement procedure, which first consisted of heating and stabilizing the sample at 400 °C for 12 h. The next step, after cooling the sample to the room temperature (RT), was the measurement aimed at determining the optimal operating temperature. This measurement was performed in the temperature range from RT to 405 °C, at a relative humidity (RH) equal to 50%. The total gas flow through the chamber was 500 sccm. The concentration of NO<sub>2</sub> applied was 20 ppm. The temperature was changed abruptly every 5 measuring cycles of 15 min/15 min (air/air + NO<sub>2</sub>). The results of this test are shown in the Figure 5a. Both samples responded best to the presence of NO<sub>2</sub> at optimal temperature.

When describing their results, the authors of the research often use the terms sensitivity and response of a gas sensor interchangeably. One of the basic parameters characterizing the gas sensor is its reaction to the gas that the sensor is to detect. Most commonly used to describe a sensor's reaction to gas is the sensor response or sensitivity. Currently, there is no uniform definition of the sensitivity (or response) of a gas sensor. Typically, the sensitivity/response (*S*) can be defined as  $R_0/R_g$  for reducing gases or  $R_g/R_0$  for oxidizing gases, where  $R_0$  is the resistance of the gas sensors in the reference gas (usually air) and  $R_g$  is the resistance in the reference gas containing the target gases. Both  $R_0$  and  $R_g$  have a significant relationship with the surface reactions taking place [49]. In this paper, this definition was used to determine the sensor's response to NO<sub>2</sub>:

$$S = \frac{R_0}{R_g} \quad (1)$$

where  $R_0$  is the sensor resistance without gas presence and  $R_g$  is the sensor resistance in the presence of gas.

Another common definition of sensitivity are the dependencies [50,51]:

$$S = \frac{R_0}{R_g} - 1 \quad (2)$$

$$S = \frac{|R_0 - R_g|}{R_g} \quad (3)$$

Scientists have different definitions of sensitivity, and the very concept of sensitivity is often used interchangeably with the sensor response. The definition adopted in this work, given by Formula (1) for the sensor's lack of response to the presence of NO<sub>2</sub> (no change in resistance), results in a value equal to 1. However, the greater the sensor's response to gas, the higher the ratio (1) gives the result. When defining the sensor response given by Formula (1), the result is always equal to (no gas response) or greater than 1.

### 2.3.2. Measurements of Electrical Properties with Alternating Current (AC)

Measurements of electrical properties by means of direct current methods are strongly disturbed by the polarization phenomena occurring in the measuring system [52]. These phenomena usually overestimate the value of the measured resistances, and in the case of low-voltage measurements, the current flow may be blocked, which makes it impossible to determine the electrical parameters of the sample [52–54]. In this case, the sample parameters calculated by the direct current methods are the sum of the electronic conductivity

processes of individual grains, the polarization processes of the intracrystalline parts and the electrode processes. For this reason, in the tested material, in order to distinguish individual parameters of each of the above-mentioned processes, which are characterized by different time constants, alternating current (AC) methods are used, e.g., impedance spectroscopy [52–54].

This method allows the understanding of the physical and chemical processes that influence the behavior of metal oxide semiconductor gas sensors, but require correct data interpretation.

The Solatron ModuLab XM measurement system was used to determine the parameters of the studied heterostructures. This system enables the determination of impedance characteristics in a wide frequencies range. The tests carried out measurements in the range from  $10^{-1}$  Hz to  $10^6$  Hz at an operating temperature of 275 °C in RH = 50%. The (AC) signal amplitude was set to 1 V. The recorded impedance spectra were analyzed using the ZView software.

#### 2.4. Material Characterization

The structural analysis of the films was carried out by an X-ray diffraction technique using PANalytical X'Pert Pro MDP with  $\text{CuK}\alpha$  ( $\lambda = 1.5406 \text{ \AA}$ ) at a step size of  $0.04^\circ$  over the  $2\theta$  range of  $30\text{--}80^\circ$ . The chemical composition of the films was confirmed by Energy Dispersive X-ray (EDS) analysis using a FEI Inspect S50 scanning electron microscope (SEM) and an X-ray energy dispersive spectrometer with Detector EDS Octane Elect Plus and Analyzer EDAX Z2-i7. In order to assure EDS measurement, the basic SEM operation parameters were that the working distance was 10 mm, the acceleration voltages of the incident electron were 5 kV and 30 kV, the electronic beam spot size was 5 and the current intensity of the incident electronic beam was about  $95 \mu\text{A}$ . Raman spectroscopy was used as a method to characterize the material tested. The Raman spectra were tested by HORIBA LabRAM HR Raman microscope with a laser treatment at 488 nm.

### 3. Results

#### 3.1. Characterization Results

The crystallographic structure of the deposited gas-sensing layers was determined with X-ray diffraction (XRD) with the special adapter to the XRD system, due to the very thin thicknesses of the copper and tin oxides. The thickness was measured by the utilization of X-ray reflectance (XRR) technique and further confirmed by the utilization of a mechanical profilometer. The estimated thickness was  $85 \text{ nm} \pm 1 \text{ nm}$ . Figure 2 shows the XRD experiment results, where peaks from CuO are observed (110,  $-111$ , 111, 020, 022, 220) from JCPD 01-072-0629 and no peaks from  $\text{SnO}_x$ , which suggests that  $\text{SnO}_x$  was not crystallized. The obtained results are in accordance with the previous results, where a higher temperature during the magnetron deposition process is required to obtain crystalline forms [55]. Moreover, the intensity of the CuO peaks is higher when CuO was deposited as a second layer, which suggests that a not-planar shape was obtained. Otherwise, the signal from the bottom layer will not be reached due to the lower X-ray measurement angle during the XRD experiments.

Regardless of the XRD measurements, to determine the composition of CuO and  $\text{SnO}_x$ , Raman spectrometry was conducted. Raman analysis detected both crystalline and amorphous phases in the sample. Raman spectra performed at 488 nm excitation contains intense peaks attributed to glass substrate ( $444 \text{ cm}^{-1}$ ,  $783 \text{ cm}^{-1}$ ,  $1099 \text{ cm}^{-1}$ ); two peaks at  $297 \text{ cm}^{-1}$  and  $361 \text{ cm}^{-1}$  can be assigned to CuO [56–58] and the peak at  $128 \text{ cm}^{-1}$  can be attributed to Sn-O, as presented in Figure 3.

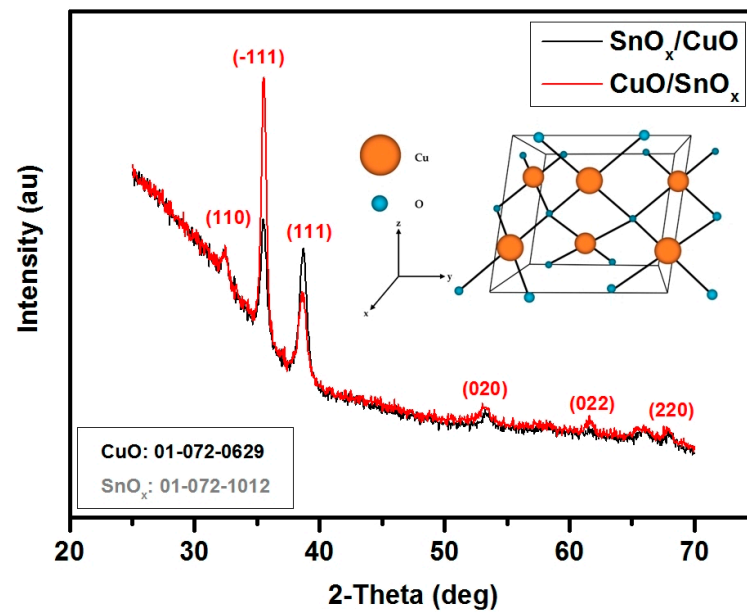


Figure 2. XRD patterns of deposited samples:  $\text{SnO}_x/\text{CuO}$  and  $\text{CuO}/\text{SnO}_x$ ; inset is the CuO monoclinic structure.

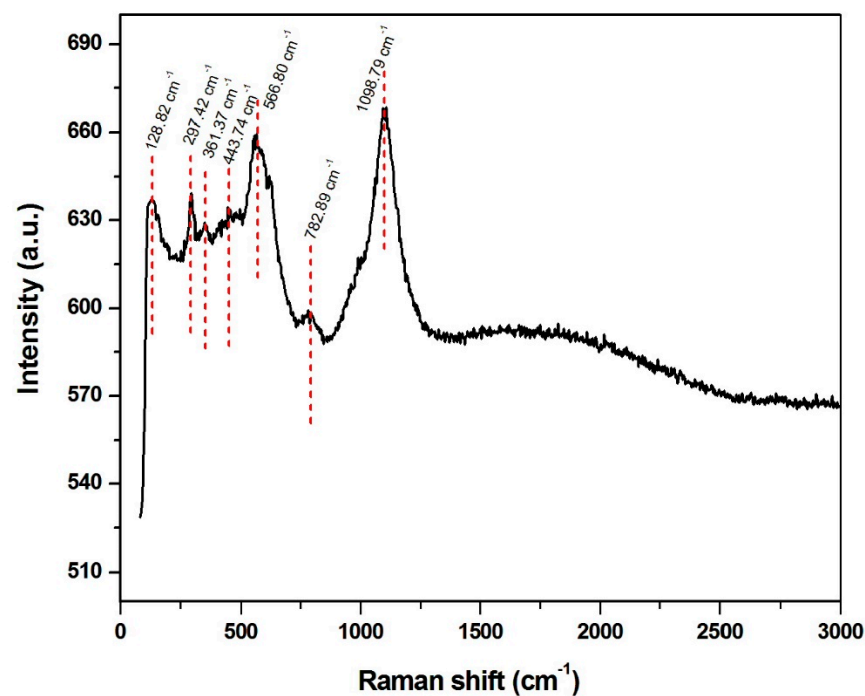


Figure 3. Raman spectra of the deposited sample  $\text{SnO}_x/\text{CuO}$ .

The morphology of the structures was investigated by scanning electron microscopy (SEM) operated at 5 kV and 30 kV. It can be seen that the surface of the sample looks uneven due to the alumina substrate effect. The analysis of the morphology of the structures indicates that the morphology of the  $\text{Al}_2\text{O}_3$  substrate is primarily visible. The  $\text{CuO}/\text{SnO}_x$  structures are too thin to be visualized in a classic SEM test. The EDS method turned out to be effective in the case of the investigated thin-layer  $\text{CuO}/\text{SnO}_x$  structures. Detailed information about the atomic structure and the elemental distribution of  $\text{SnO}_x\text{-CuO}$  stack was obtained by SEM and, in combination with EDS, for elemental analysis resolution. The EDS experiments results have shown solely the presence of Cu, Sn and O. As shown in the

elemental map, obtained by EDS analysis (Figure 4), the sensing structure consists of Sn, Cu and O (explained in caption of Figure 4), indicating the uniform formation of  $\text{SnO}_x/\text{CuO}$ .

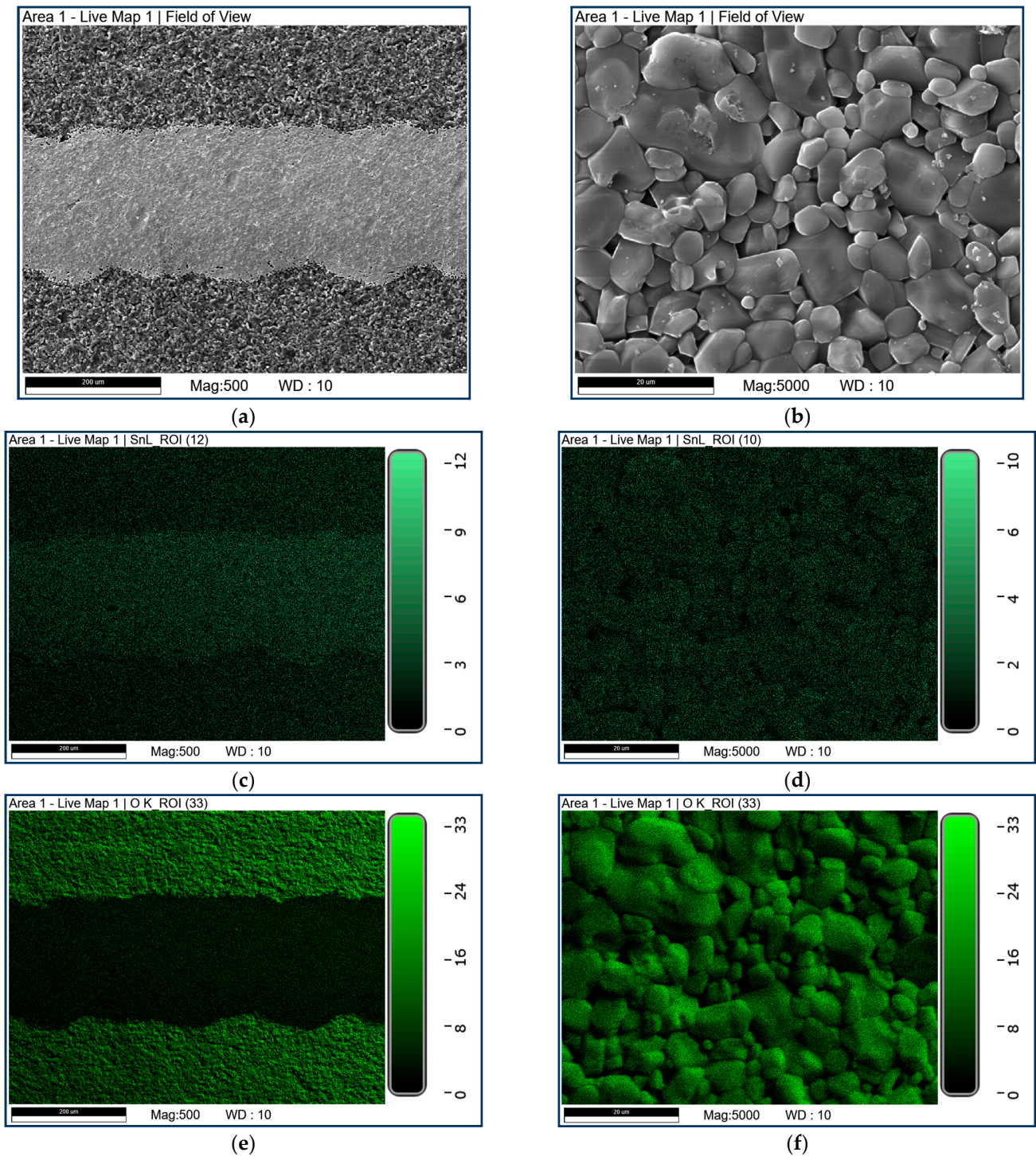
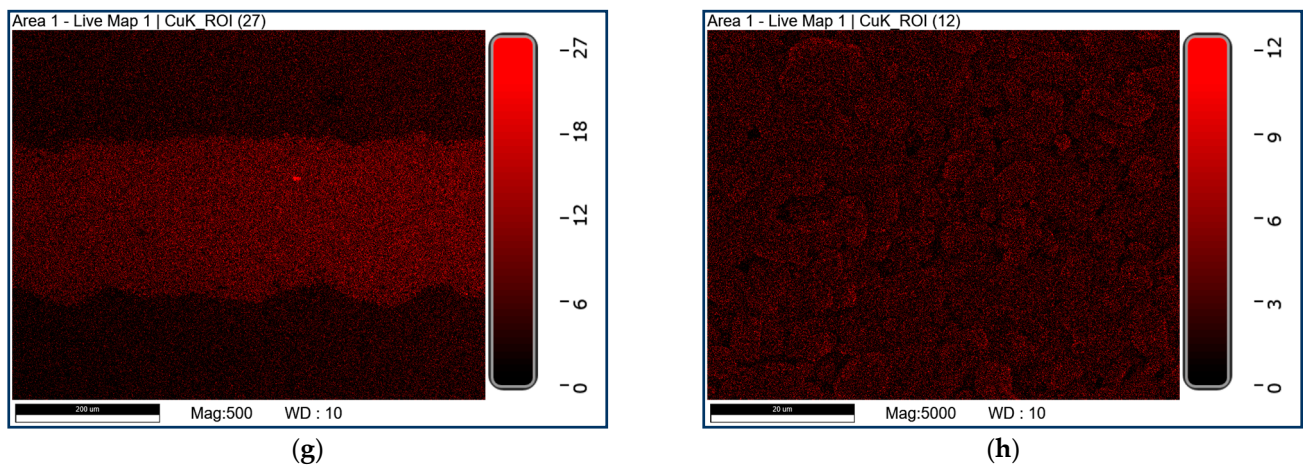


Figure 4. Cont.



**Figure 4.** SEM and EDS results of CuO/SnO<sub>x</sub> sample: (a) SEM image of the area from the Figure 1a where the deposited gas sensitive layer on the electrode is illustrated; (b) zoom of image 4a to the gas sensor material; (c) EDS map of Sn from image (a); (d) zoom of image 4c to the gas sensor material; (e) EDS map of O from image 4a; (f) zoom of image 4e to the gas sensor material; (g) EDS map of Cu from image (a); (h) zoom of image 4g to the gas sensor material. The scales indicate the counts of the EDS signal.

### 3.2. Gas-Sensing Characteristics

#### 3.2.1. NO<sub>2</sub>

The first experiments were conducted to determine the optimal operating temperature of the samples, i.e., SnO<sub>x</sub>/CuO and CuO/SnO<sub>x</sub>. As can be observed (Figure 5a), the maximal response was obtained around 250 °C for both cases; for SnO<sub>x</sub>/CuO, it was 240 °C and for CuO/SnO<sub>x</sub>, it was 275 °C. Therefore, further experiments were conducted at the optimal operating temperatures. The calibration curves (0.5–20 ppm of NO<sub>2</sub>) were presented in Figure 5b, and measurement data were fitted with  $A_1 - A_2e^{-kx}$  formula with  $R^2 = 0.97278$  and  $0.96837$  for SnO<sub>x</sub>/CuO and CuO/SnO<sub>x</sub>, respectively. The effect of relative humidity (30%, 50%, 70%) with NO<sub>2</sub> (0.5–20 ppm) is presented in Figure 5c,d. However, for both cases, increased RH level resulted in an increased response.

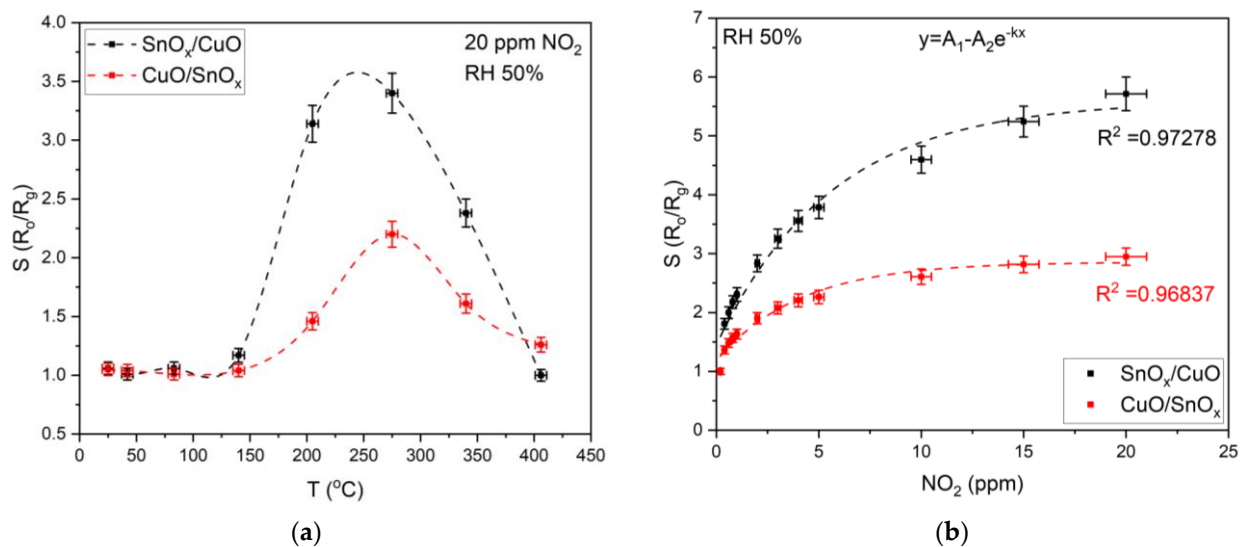


**Figure 5.** Cont.

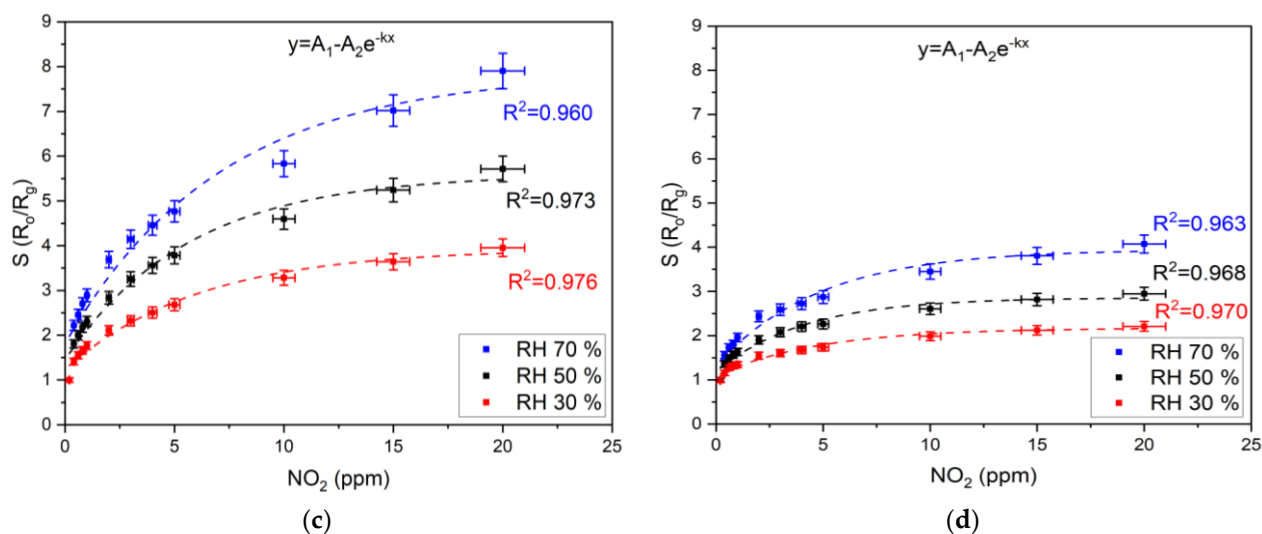


**Figure 5.** Sensor test results. (a) Sample response to 20 ppm  $NO_2$  at 50% RH as a function of temperature. (b) The response of samples at optimal temperature to various concentrations of  $NO_2$  from 0.5 ppm to 20 ppm at 50% RH. (c)  $SnO_x/CuO$  sample responses to different  $NO_2$  concentrations depending on RH. (d)  $CuO/SnO_x$  sample responses to different  $NO_2$  concentrations depending on RH.

Within the study, the multi-test was performed to verify the stability of the samples over time. Figure 6a for the  $SnO_x/CuO$  sample and Figure 5b for the  $CuO/SnO_x$  sample show the results of measurements of changes in sensor resistance for three measurement cycles 60 min/60 min (air/air +  $NO_2$ ) at different concentrations of  $NO_2$  in the range of 0.5–5.0 ppm. The measurements were made at the optimum operating temperatures (Figure 5a) and 50% RH. For the  $NO_2$  concentration equal to 5 ppm, a stability test was carried out for 10 measurement cycles of 30 min/30 min (air/air +  $NO_2$ ) at the optimal temperature and RH 50%. The results for individual samples are presented in Figure 5c,d. Figure 6c,d show the results of the stable operation tests for both samples consisting of 10 cycles of 30 min/30 min (air/air +  $NO_2$ ) each. Measurements on each of the samples were carried out for several weeks at different temperatures, RH levels and  $NO_2$  concentrations; during this time, no change in sensor properties of the samples was observed. Both samples exhibited good stability over time.

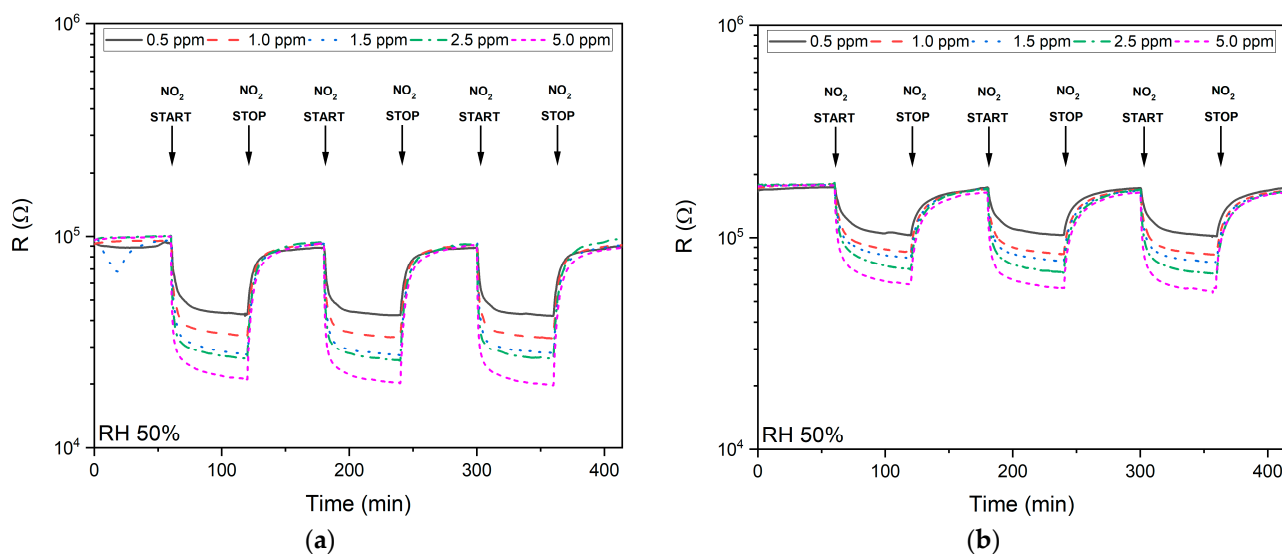


**Figure 6.** Cont.

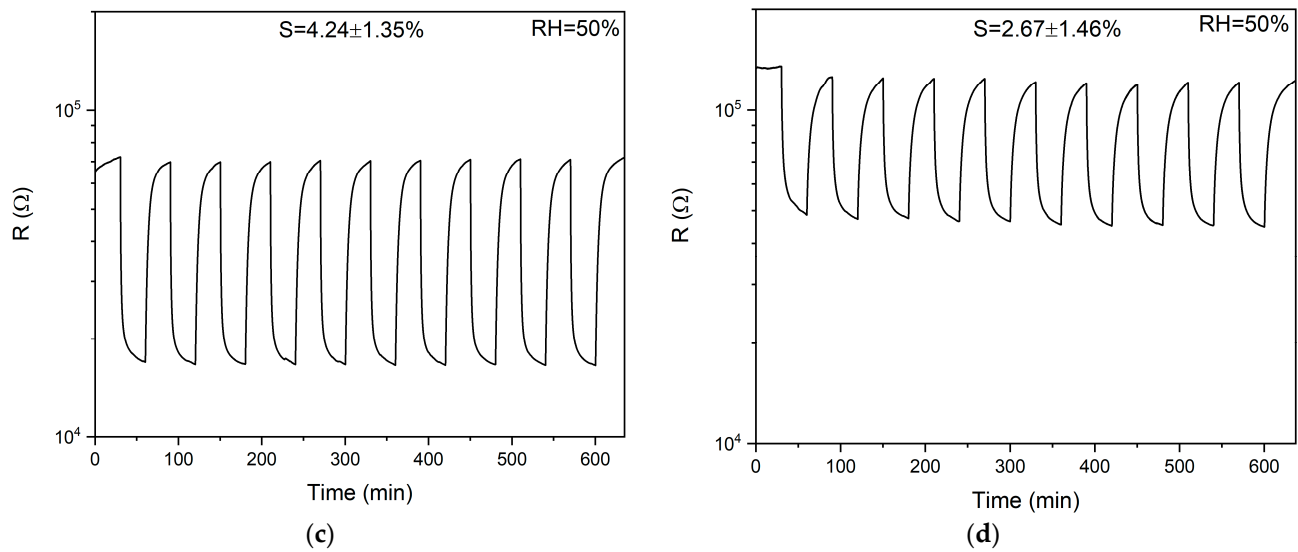


**Figure 6.** The results of measurements of the stability of the sensors. (a) Changes in the  $\text{SnO}_x/\text{CuO}$  sample resistance at different concentrations of  $\text{NO}_2$ . (b) Changes in the resistance of the  $\text{CuO}/\text{SnO}_x$  sample at different concentrations of  $\text{NO}_2$ . (c) The stability of the  $\text{SnO}_x/\text{CuO}$  sample at the optimum temperature at 10 measuring cycles. (d) The stability of the  $\text{CuO}/\text{SnO}_x$  sample at the optimum temperature at 10 measuring cycles.

The impedance spectra in Nyquist representation ( $Z''$  plotted against  $Z'$ ) for the prepared sample of  $\text{SnO}_x/\text{CuO}$  and  $\text{CuO}/\text{SnO}_x$  in the optimal operating temperature in air and under  $\text{NO}_2$  exposure (0.5–5 ppm) are shown in Figure 7. It was also observed that the diameter of the circle decreased when the  $\text{NO}_2$  admission was increased.

Nyquist plots show the imaginary part of  $Z'$  as a function of the real part  $Z''$  (Figure 7a,b). In order to develop a suitable surrogate model of an electrical circuit, samples need to be analyzed over a wide frequency range. Distribution of the absolute fit error is included in Figure 8 below the Bode and Nyquist plots. The decreasing impedance with increasing frequency is evidence of the increasing conductivity of the sample. The Supplementary Materials contain plots of frequency characteristics of the phase, Bode representations (Figure S1), which are complementary to Figure 7a,c.

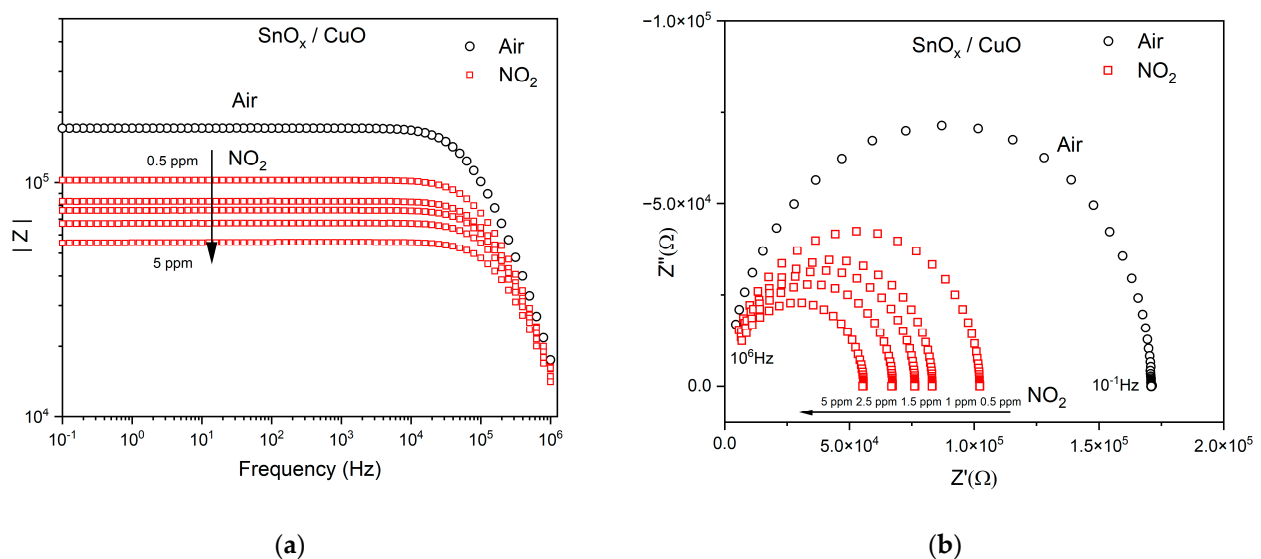
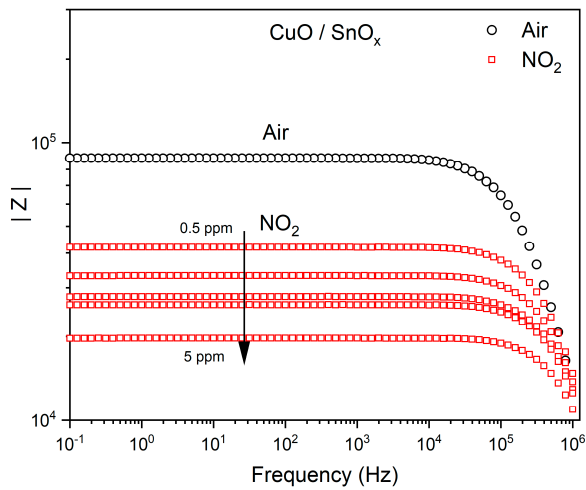
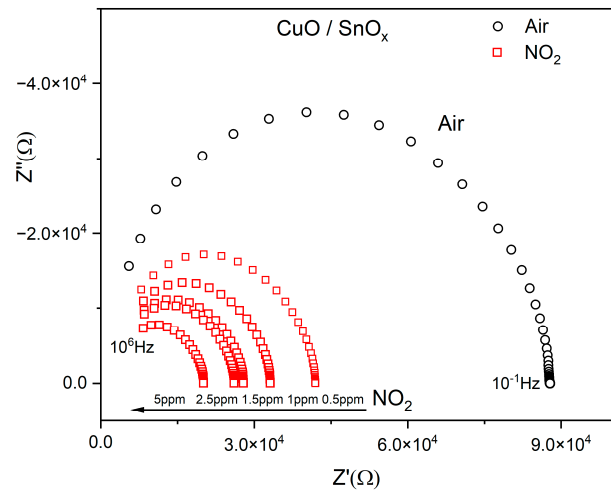


**Figure 7.** Cont.

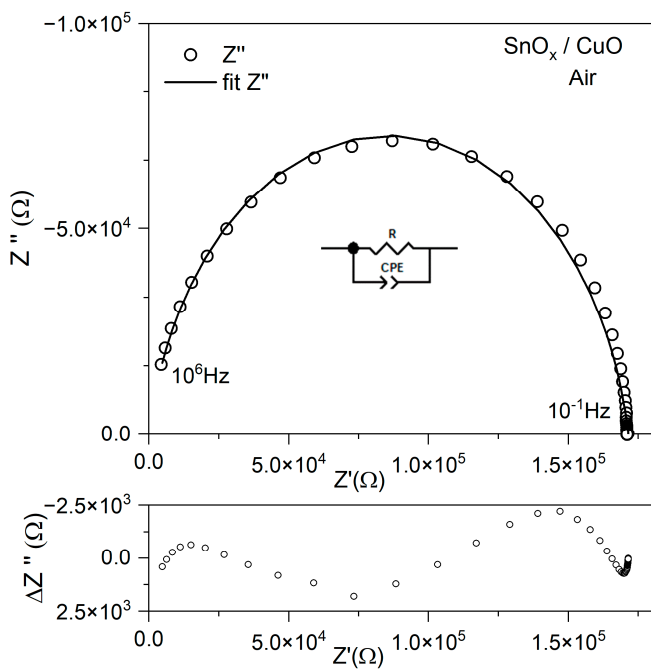


(c)

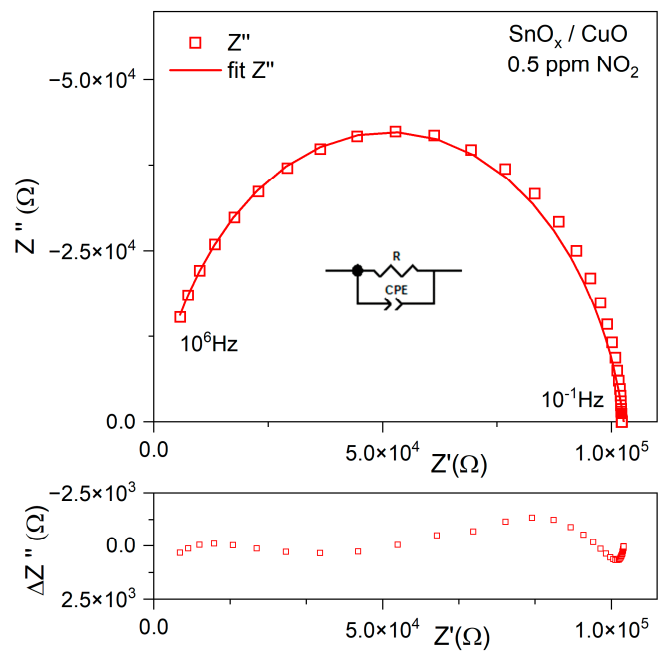


(d)

**Figure 7.** Impedance spectra of the nanomaterials in operating temperature of 275 °C in air and upon NO<sub>2</sub> admission (0.5–5 ppm): (a) Bode representation SnO<sub>x</sub>/CuO; (b) Nyquist representation SnO<sub>x</sub>/CuO; (c) Bode representation CuO/SnO<sub>x</sub>; (d) Nyquist representation CuO/SnO<sub>x</sub>.



(a)



(b)

**Figure 8.** Cont.

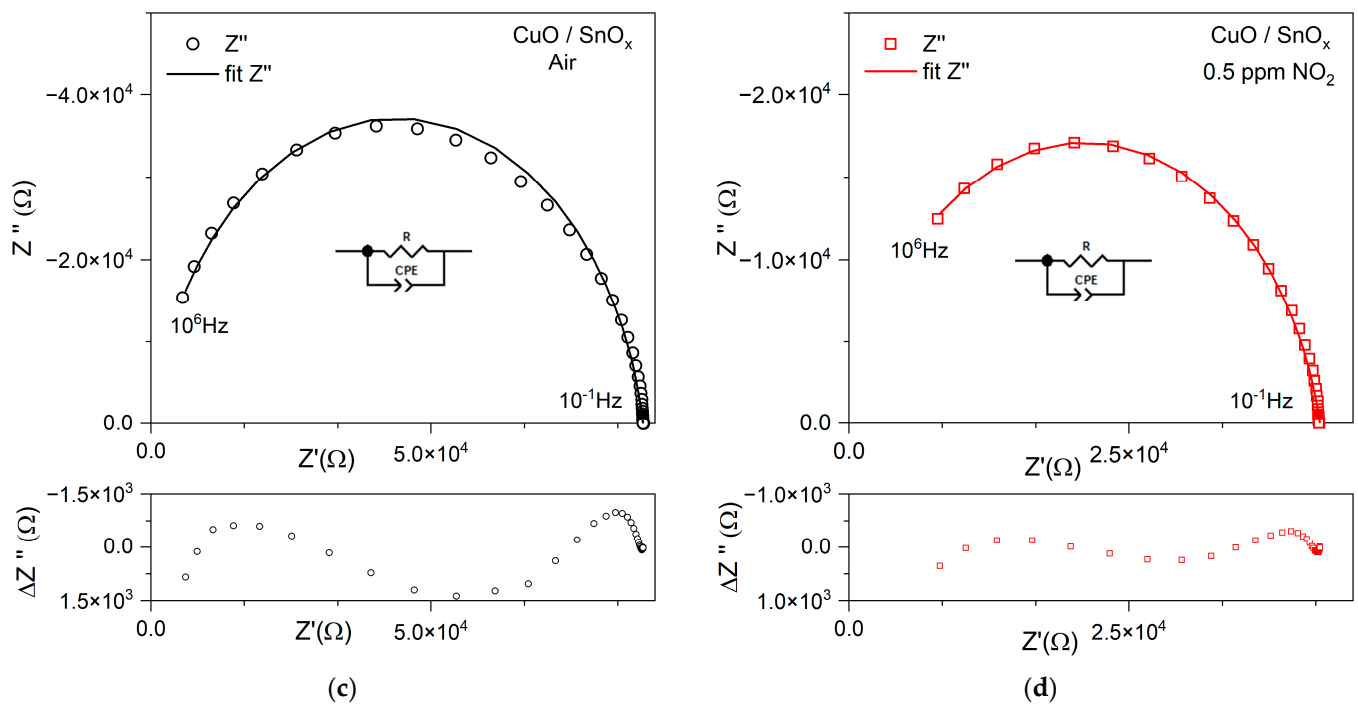


**Figure 8.** Impedance plots in Nyquist representation for SnO<sub>x</sub>/CuO and SnO<sub>x</sub>/CuO nanomaterials in measurement a very wide frequency range and electrical equivalent circuit. (a) SnO<sub>x</sub>/CuO in air atmosphere; (b) SnO<sub>x</sub>/CuO upon 0.5 ppm NO<sub>2</sub> admission; (c) SnO<sub>x</sub>/CuO in air atmosphere; (d) SnO<sub>x</sub>/CuO upon 0.5 ppm NO<sub>2</sub> admission. Distribution of the absolute fit error is included below the Bode and Nyquist plots.

A simple replacement model was used to describe the frequency characteristics of the obtained thin films as a function of NO<sub>2</sub> concentration.

Based on the results of matching the impedance spectra, a substitute model consisting of R and constant phase element (CPE) elements connected in parallel were proposed. The CPE is defined according to the following equation [53]:

$$Z_{\text{CPE}} = [A(j\omega)^\alpha]^{-1} \quad (4)$$

The constant marked with the letter  $A$  defines the impedance modulus. The  $\alpha$ , which is in the exponent, represents the impedance angle range (from 0° to 90°). In the case where the  $\alpha$  value is equal to 90°, the CPE is defined as a capacitor with a capacitance equal to  $A$ . In the case where  $\alpha$  is equal to 0, we can assume that the element is resistance. The main effect of this function in an impedance plot is to distort the semicircle.

The CPE is a distributed element that produces an impedance having a constant phase angle in the complex plane [52]. With received characteristics, it can be concluded that the electric resistance  $R$  of tested thin films reacts to the presence of nitrogen dioxide. In the analyzed cases, the  $P$  (phase) parameter of the CPE element takes values in the range of 0.90–0.95, which correspond to the capacity. The mechanisms of electronic or ionic conduction are represented by the resistive element ( $R$ ). Capacitance ( $C$ ) represents the sample's polarizability in various areas of the material structure, which takes place inside the grain, at their boundaries and at the electrodes [59].

Parameters of the electrical equivalent circuit for SnO<sub>x</sub>/CuO, in air:  $R = (1.71 \pm 0.02) \cdot 10^5$  Ohm,  $\text{CPE-A} = (4.46 \pm 0.07) \cdot 10^{-11}$  F,  $\text{CPE-P} = 0.89 \pm 0.01$ ; upon 0.5 ppm NO<sub>2</sub> admission:  $R = (1.03 \pm 0.04) \cdot 10^5$  Ohm,  $\text{CPE-A} = (7.20 \pm 0.06) \cdot 10^{-11}$  F,  $\text{CPE-P} = (0.86 \pm 0.01)$ . Parameters of the electrical equivalent circuit for CuO/SnO<sub>x</sub>, in air:  $R = (0.92 \pm 0.01) \cdot 10^5$  Ohm,  $\text{CPE-A} = (4.38 \pm 0.11) \cdot 10^{-11}$  F,  $\text{CPE-P} = 0.90 \pm 0.01$ ; upon 0.5 ppm NO<sub>2</sub> admission:  $R = (0.47 \pm 0.01) \cdot 10^5$  ohm,  $\text{CPE-A} = (6.93 \pm 0.01) \cdot 10^{-11}$  F,  $\text{CPE-P} = (0.87 \pm 0.01)$ .

The determined parameters of the substitute model allow us to determine the influence of the participation of particular phases of the structure—granular and intergranular conductivity and electrode processes—in the gas detection mechanisms.

### 3.2.2. VOCs

The deposited gas-sensing layers were tested for cross-sensitivity under exposure to various VOCs such as acetone, ethanol and propane, as well as under various concentrations of relative humidity. The results are given in Figure 9. As can be observed in the 0.5–2.0 ppm range, the gas sensors result in no response to VOCs. Moreover, thanks to the p-n and n-p structures, the response to various RHs is more stable in comparison with typical single structure responses of MOX-based gas sensors, i.e., CuO-based and SnO-based.

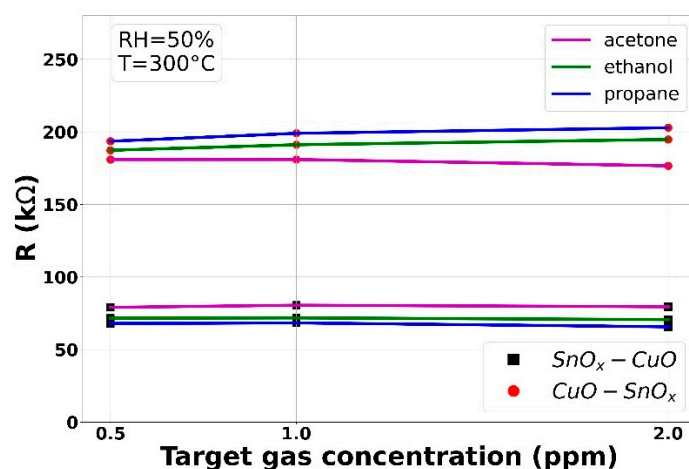
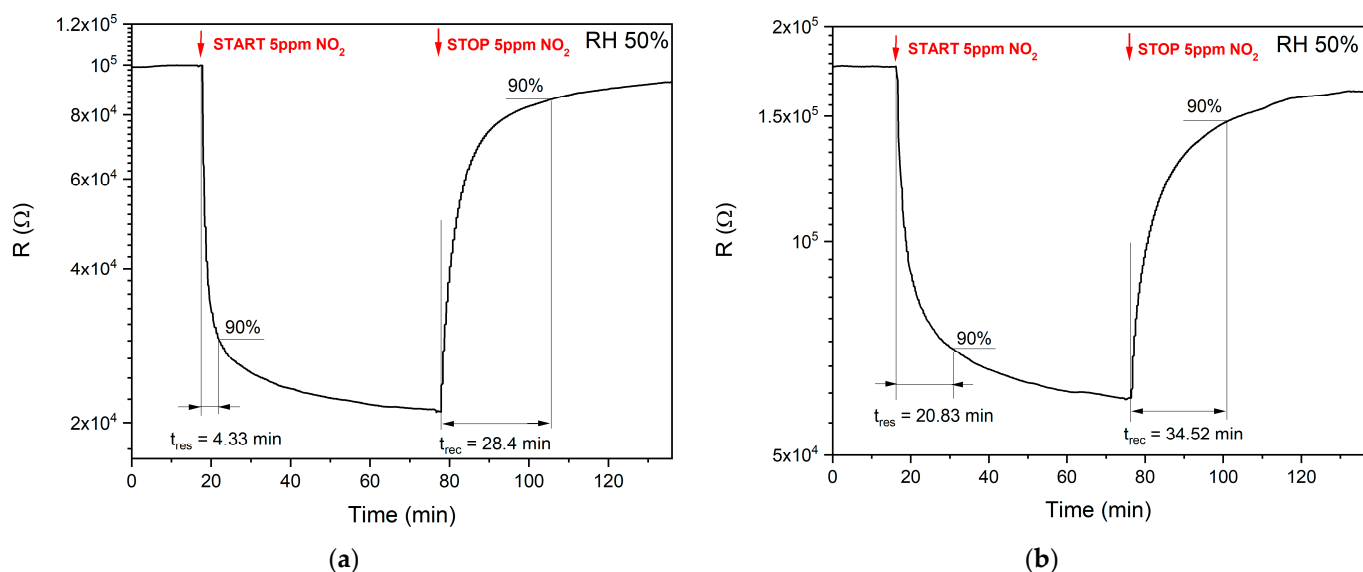


Figure 9. The gas-sensing results of the samples after exposure to various VOCs and relative humidity.

### 3.2.3. Response and Recovery Times

Regardless of the sensitivity and selectivity, the gas sensors are also characterized by response and recovery time(s). A good method for response and recovery times calculations was given by Zhang et al. [60]. Usually, the 10–90% range of the signal changes is used for determining these times. However, within this study, the developed gas sensors were tested in the measurement setup that was designed for air-pollution monitoring in the specific industrial application which is classified. Therefore, the simple comparison between obtained responses and responses reported in other studies cannot be conducted. During the determination of the response and recovery times, the sensors were tested in cycles lasting 60 min/60 min (air/air + NO<sub>2</sub>). For such long measurement cycles, it is possible to assume a relatively steady state of the sensor operation after nearly one hour of operation in constant conditions of the presence or absence of NO<sub>2</sub> in the measuring chamber. The concentration of NO<sub>2</sub> was 5 ppm. The samples operated at the optimum operating temperature and a relative humidity of 50%. Figure 10a shows the response and recovery time determination method for the SnO<sub>x</sub>/CuO sample and Figure 10b shows this for the CuO/SnO<sub>x</sub> sample.

Interestingly, the developed gas sensors based on SnO<sub>x</sub>/CuO composition exhibited both higher and faster NO<sub>2</sub> response, while recovery times were comparable. Therefore, the SnO<sub>x</sub>/CuO structure is preferred and further experiments will be conducted to define an optimal ratio between both materials.



**Figure 10.** The measurement of response and recovery times. (a) Full 60min/60min measurement cycle (air/air +  $\text{NO}_2$ ) at RH 50% at the optimum temperature of 275 °C with response and recovery times for the  $\text{SnO}_x/\text{CuO}$  sample marked. (b) Full 60min/60min measurement cycle (air/air +  $\text{NO}_2$ ) at RH 50% at the optimum temperature of 275 °C with response and recovery times for the  $\text{CuO}/\text{SnO}_x$  sample marked.

#### 4. Conclusions

The analysis of air pollutants is currently one of the burning tasks. Thanks to technical developments, fabrication of the gas sensors based on chemo resistive structures are cheap and could be an effective way to include the sensors in many applications, including the automotive industry. However, the environmental conditions are challenging in such applications, and therefore, novel realizations are a subject of research, including heterostructures of semiconductors. In this paper, we report the research results on  $\text{CuO}/\text{SnO}_x$  and  $\text{SnO}_x/\text{CuO}$  structures under exposure to various concentrations of  $\text{NO}_2$ , as well as VOCs. The gas-sensitive layers were deposited with the utilization of the glancing angle sputtering deposition technique that offers a uniform distribution of the material; however, to provide a stable substrate for demanding conditions, such as working in the cars, the alumina substrates were used. The alumina substrates are characterized by high thermal and chemical stability, and the developed sensors have also shown good stability, selectivity and sensitivity to  $\text{NO}_2$  in the 0.5–20 ppm range, which covers the concentrations in the air. Thanks to the heterostructure composition, the sensors work well in the 30–70% RH range, and  $\text{SnO}_x/\text{CuO}$  showed a higher response at lower temperatures. The drawback of the developed sensors is the higher response time; however, the measurement setup was not optimized for this issue. The authors of the paper are working on creating an electronic nose in which many gas sensors will work in a microsystem. The developed sensors showed in this article will be used as a part of the mentioned microsystem and gas-dosing parts will be further optimized. The entire electronic nose system will be presented in another article, as will other sensors included in the microsystem. Nevertheless, the obtained results are very promising.

**Supplementary Materials:** The following are available online at <https://www.mdpi.com/article/10.3390/s21134387/s1>, Figure S1: Impedance spectra of the nanomaterials in operating temperature of 275 °C in air and upon  $\text{NO}_2$  admission (0.5 ppm–5 ppm): (a) Bode representation  $\text{SnO}_x/\text{CuO}$ ; (b) Bode representation  $\text{CuO}/\text{SnO}_x$ .

**Author Contributions:** Conceptualization, A.P., A.B., D.G., A.R.; methodology, A.P., B.S., Ł.F., D.G.; software, A.P., D.G.; validation, S.K., M.J.-S., E.M., P.K., A.R.; formal analysis E.M., A.R., investigation, A.P., B.S., Ł.F., D.G., S.K., M.J.-S., E.M., P.K., A.R., data curation, A.P., B.S., Ł.F., D.G., S.K., M.J.-S., E.M., P.K., A.R., writing—original draft preparation A.P., B.S., Ł.F., D.G., A.R.; writing—review and editing

A.P., B.S., L.F., D.G., S.K., M.J.-S., E.M., P.K., A.R.; visualization A.P., B.S., L.F., D.G., S.K., M.J.-S., E.M., P.K.; supervision, A.R., project administration, A.R., funding acquisition A.R. All authors have read and agreed to the published version of the manuscript.

**Funding:** The research leading to these results received funding from the Norway Grants 2014–2021 via the National Centre for Research and Development.

**Institutional Review Board Statement:** Not applicable.

**Informed Consent Statement:** Not applicable.

**Data Availability Statement:** Not applicable.

**Conflicts of Interest:** The authors declare no conflict of interest.

## References

1. Gas Sensor Market Size, Share | Industry Trends and Growth by 2027. Available online: <https://www.alliedmarketresearch.com/gas-sensors-market> (accessed on 6 February 2021).
2. Gas Sensors Market by Analysis, Type, Technology, Technology, Output Type, Product Type, Application | COVID-19 Impact Analysis | MarketsandMarketsTM. Available online: <https://www.marketsandmarkets.com/Market-Reports/gas-sensor-market-245141093.html> (accessed on 13 April 2021).
3. Global Gas Sensor Market Size & Share Report, 2021–2028. Available online: <https://www.grandviewresearch.com/industry-analysis/gas-sensors-market> (accessed on 6 February 2021).
4. WHO. Formaldehyde. In *Selected Pollutants. WHO Guidelines for Indoor Air Quality*; WHO, Regional Office for Europe: Copenhagen, Denmark, 2010; pp. 103–156. ISBN 978-92-890-02134. Available online: [http://www.euro.who.int/\\_\\_data/assets/pdf\\_file/0009/128169/e94535.pdf?ua=1](http://www.euro.who.int/__data/assets/pdf_file/0009/128169/e94535.pdf?ua=1) (accessed on 6 April 2021).
5. World Health Organization. Ambient (Outdoor) Air Pollution. Available online: [https://www.who.int/news-room/fact-sheets/detail/ambient-\(outdoor\)-air-quality-and-health](https://www.who.int/news-room/fact-sheets/detail/ambient-(outdoor)-air-quality-and-health) (accessed on 3 March 2020).
6. EUR-Lex—L:2008:152:TOC—EN—EUR-Lex. Available online: <https://eur-lex.europa.eu/legal-content/EN/TXT/?uri=OJ:L:2008:152:TOC> (accessed on 14 April 2021).
7. CDC—Immediately Dangerous to Life or Health Concentrations (IDLH): Nitrogen Dioxide—NIOSH Publications and Products. Available online: <https://www.cdc.gov/niosh/idlh/10102440.html> (accessed on 16 April 2021).
8. Commission Regulation (EU) 2018/1832 of 5 November 2018 Amending Directive 2007/46/EC of the European Parliament and of the Council, Commission Regulation (EC) No 692/2008 and Commission Regulation (EU) 2017/1151 for the Purpose of Improving the Emission Type Approval Tests and Procedures for Light Passenger and Commercial Vehicles, Including Those for in-Service Conformity and Real-Driving Emissions and Introducing Devices for Monitoring the Consumption of Fuel and Electric Energy (Text with EEA Relevance). 2018, Volume 301. Available online: <https://eur-lex.europa.eu/legal-content/EN/TXT/PDF/?uri=CELEX:32018R1832&from=FR> (accessed on 7 April 2021).
9. Directive 2012/13/EU of the European Parliament and of the Council of 22 May 2012 on the Right to Information in Criminal Proceedings. 2012. Available online: <https://eur-lex.europa.eu/legal-content/EN/TXT/?uri=CELEX:32012L0013> (accessed on 7 April 2021).
10. EUR-Lex—32012R0459—EN—EUR-Lex. Available online: <https://eur-lex.europa.eu/eli/reg/2012/459/oj> (accessed on 17 April 2021).
11. Ligterink, N.E.; Kadijk, G.A.; Mensch, P.V.; Smokers, R.T.M. *NOx Emissions of Euro 5 and Euro 6 Diesel Passenger Cars—Test Results in the Lab and on the Road*; TNO: Delft, The Netherlands, 2016. [CrossRef]
12. Aleixandre, M.; Gerboles, M. Review of Small Commercial Sensors for Indicative Monitoring of Ambient Gas. *Chem. Eng. Trans.* **2012**, *30*, 1–6.
13. Choi, M.S.; Gil Na, H.; Mirzaei, A.; Bang, J.H.; Oum, W.; Han, S.; Choi, S.-W.; Kim, M.; Jin, C.; Kim, S.S.; et al. Room-temperature NO<sub>2</sub> sensor based on electrochemically etched porous silicon. *J. Alloys Compd.* **2019**, *811*, 151975. [CrossRef]
14. Zhao, J.; Wen, X.; Huang, Y.; Liu, P. Piezoelectric circuitry tailoring for resonant mass sensors providing ultra-high impedance sensitivity. *Sens. Actuators A Phys.* **2019**, *285*, 275–282. [CrossRef]
15. Wasisto, H.S.; Merzsch, S.; Stranz, A.; Waag, A.; Uhde, E.; Salthammer, T.; Peiner, E. Silicon resonant nanopillar sensors for airborne titanium dioxide engineered nanoparticle mass detection. *Sens. Actuators B Chem.* **2013**, *189*, 146–156. [CrossRef]
16. Jia, H.; Xu, P.; Li, X. Integrated Resonant Micro/Nano Gravimetric Sensors for Bio/Chemical Detection in Air and Liquid. *Micromachines* **2021**, *12*, 645. [CrossRef]
17. Alunda, B.O.; Lee, Y.J. Review: Cantilever-Based Sensors for High Speed Atomic Force Microscopy. *Sensors* **2020**, *20*, 4784. [CrossRef]
18. Zhao, J.; Sun, C.; Kacem, N.; Wang, H.; Gao, R.; Liu, P.; Huang, Y. A nonlinear resonant mass sensor with enhanced sensitivity and resolution incorporating compressed bistable beam. *J. Appl. Phys.* **2018**, *124*, 164503. [CrossRef]
19. Akbari, E.; Jahanbin, K.; Afroozeh, A.; Yupapin, P.; Buntat, Z. Brief review of monolayer molybdenum disulfide application in gas sensor. *Phys. B Condens. Matter* **2018**, *545*, 510–518. [CrossRef]

20. Rana, M.; Ibrahim, D.S.; Asyraf, M.M.; Jarin, S.; Tomal, A. A review on recent advances of CNTs as gas sensors. *Sens. Rev.* **2017**, *37*, 127–136. [[CrossRef](#)]
21. Toda, K.; Furue, R.; Hayami, S. Recent progress in applications of graphene oxide for gas sensing: A review. *Anal. Chim. Acta* **2015**, *878*, 43–53. [[CrossRef](#)]
22. Nikolic, M.V.; Milovanovic, V.; Vasiljevic, Z.Z.; Stamenkovic, Z. Semiconductor Gas Sensors: Materials, Technology, Design, and Application. *Sensors* **2020**, *20*, 6694. [[CrossRef](#)]
23. Dey, A. Semiconductor metal oxide gas sensors: A review. *Mater. Sci. Eng. B* **2018**, *229*, 206–217. [[CrossRef](#)]
24. Nazemi, H.; Joseph, A.; Park, J.; Emadi, A. Advanced Micro- and Nano-Gas Sensor Technology: A Review. *Sensors* **2019**, *19*, 1285. [[CrossRef](#)]
25. Zhang, C.; Liu, G.; Geng, X.; Wu, K.; Debliquy, M. Metal oxide semiconductors with highly concentrated oxygen vacancies for gas sensing materials: A review. *Sens. Actuators A Phys.* **2020**, *309*, 112026. [[CrossRef](#)]
26. Hung, C.M.; Le, D.T.T.; Van Hieu, N. On-chip growth of semiconductor metal oxide nanowires for gas sensors: A review. *J. Sci. Adv. Mater. Devices* **2017**, *2*, 263–285. [[CrossRef](#)]
27. Comini, E. Metal oxides nanowires chemical/gas sensors: Recent advances. *Mater. Today Adv.* **2020**, *7*, 100099. [[CrossRef](#)]
28. Yang, S.; Lei, G.; Xu, H.; Lan, Z.; Wang, Z.; Gu, H. Metal Oxide Based Heterojunctions for Gas Sensors: A Review. *Nanomaterials* **2021**, *11*, 1026. [[CrossRef](#)]
29. Wang, Y.; Duan, L.; Deng, Z.; Liao, J. Electrically Transduced Gas Sensors Based on Semiconducting Metal Oxide Nanowires. *Sensors* **2020**, *20*, 6781. [[CrossRef](#)]
30. Zappa, D.; Galstyan, V.; Kaur, N.; Arachchige, H.M.M.; Sisman, O.; Comini, E. “Metal oxide -based heterostructures for gas sensors”—A review. *Anal. Chim. Acta* **2018**, *1039*, 1–23. [[CrossRef](#)]
31. Szafraniak, B.; Fušnik, L.; Xu, J.; Gao, F.; Brudnik, A.; Rydosz, A. Semiconducting Metal Oxides: SrTiO<sub>3</sub>, BaTiO<sub>3</sub> and BaSrTiO<sub>3</sub> in Gas-Sensing Applications: A Review. *Coatings* **2021**, *11*, 185. [[CrossRef](#)]
32. Ciobota, C.; Piticescu, R.; Neagoe, C.; Tudor, I.; Matei, A.; Dragut, D.; Sobetkii, A.; Anghel, E.; Stanoiu, A.; Simion, C.; et al. Nanostructured Cobalt Doped Barium Strontium Titanate Thin Films with Potential in CO<sub>2</sub> Detection. *Materials* **2020**, *13*, 4797. [[CrossRef](#)]
33. Hu, Y.; Tan, O.K.; Cao, W.; Zhu, W. A low temperature nano-structured SrTiO<sub>3</sub> thick film oxygen gas sensor. *Ceram. Int.* **2004**, *30*, 1819–1822. [[CrossRef](#)]
34. Maziarz, W.; Rydosz, A.; Pisarkiewicz, T.; Domański, K.; Grabiec, P. Gas-sensitive Properties of ZnO Nanorods/Nanowires Obtained by Electrodeposition and Electrospinning Methods. *Procedia Eng.* **2012**, *47*, 841–844. [[CrossRef](#)]
35. Rydosz, A.; Staszek, K.; Brudnik, A.; Gruszczynski, S. Tin Dioxide Thin Film with UV-enhanced Acetone Detection in Microwave Frequency Range. *Micromachines* **2019**, *10*, 574. [[CrossRef](#)]
36. Rydosz, A.; Dymała, K.; Kollbek, K.; Andrysiewicz, W.; Sitarz, M.; Marszałek, K. Structure and optical properties of the WO<sub>3</sub> thin films deposited by the GLAD magnetron sputtering technique. *Vacuum* **2020**, *177*, 109378. [[CrossRef](#)]
37. Rydosz, A.; Dymała, K.; Andrysiewicz, W.; Grochala, D.; Marszałek, K. GLAD Magnetron Sputtered Ultra-Thin Copper Oxide Films for Gas-Sensing Application. *Coatings* **2020**, *10*, 378. [[CrossRef](#)]
38. Eranna, G. *Metal Oxide Nanostructures as Gas Sensing Devices*; Informa UK Limited: London, UK, 2016.
39. Sun, Y.-F.; Liu, S.-B.; Meng, F.-L.; Liu, J.-H.; Jin, Z.; Kong, L.-T. Metal Oxide Nanostructures and Their Gas Sensing Properties: A Review. *Sensors* **2012**, *12*, 2610–2631. [[CrossRef](#)]
40. Bag, A.; Lee, N.-E. Gas sensing with heterostructures based on two-dimensional nanostructured materials: A review. *J. Mater. Chem. C* **2019**, *7*, 13367–13383. [[CrossRef](#)]
41. Pisarkiewicz, T.; Maziarz, W.; Małolepszy, A.; Stobiński, L.; Michoń, D.A.; Szkudlarek, A.; Pisarek, M.; Kanak, J.; Rydosz, A. Nitrogen Dioxide Sensing using Multilayer Structure of Reduced Graphene Oxide and  $\alpha$ -Fe<sub>2</sub>O<sub>3</sub>. *Sensors* **2021**, *21*, 1011. [[CrossRef](#)]
42. Alev, O.; Kılıç, A.; Çakırlar, Ç.; Büyükköse, S.; Öztürk, Z.Z. Gas Sensing Properties of p-Co<sub>3</sub>O<sub>4</sub>/n-TiO<sub>2</sub> Nanotube Heterostructures. *Sensors* **2018**, *18*, 956. [[CrossRef](#)]
43. Chatterjee, S.G.; Chatterjee, S.; Ray, A.K.; Chakraborty, A.K. Graphene–metal oxide nanohybrids for toxic gas sensor: A review. *Sens. Actuators B Chem.* **2015**, *221*, 1170–1181. [[CrossRef](#)]
44. Kurt, J. Lesker Company. Available online: [https://www.lesker.com/newweb/deposition\\_materials/depositionmaterials\\_sputtertargets\\_1.cfm?pgid=cu1](https://www.lesker.com/newweb/deposition_materials/depositionmaterials_sputtertargets_1.cfm?pgid=cu1) (accessed on 29 April 2021).
45. Rydosz, A.; Brudnik, A.; Staszek, K. Metal Oxide Thin Films Prepared by Magnetron Sputtering Technology for Volatile Organic Compound Detection in the Microwave Frequency Range. *Materials* **2019**, *12*, 877. [[CrossRef](#)] [[PubMed](#)]
46. Rydosz, A. The Use of Copper Oxide Thin Films in Gas-Sensing Applications. *Coatings* **2018**, *8*, 425. [[CrossRef](#)]
47. Rydosz, A.; Kollbek, K.; Kim-Ngan, N.-T.H.; Czapl, A.; Brudnik, A. Optical diagnostics of the magnetron sputtering process of copper in an argon–oxygen atmosphere. *J. Mater. Sci. Mater. Electron.* **2020**, *31*, 11624–11636. [[CrossRef](#)]
48. Pisarkiewicz, T.; Maziarz, W.; Małolepszy, A.; Stobiński, L.; Michoń, D.; Rydosz, A. Multilayer Structure of Reduced Graphene Oxide and Copper Oxide as a Gas Sensor. *Coatings* **2020**, *10*, 1015. [[CrossRef](#)]
49. Wang, C.; Yin, L.; Zhang, L.; Xiang, D.; Gao, R. Metal Oxide Gas Sensors: Sensitivity and Influencing Factors. *Sensors* **2010**, *10*, 2088–2106. [[CrossRef](#)]

50. Dufour, N.; Veyrac, Y.; Menini, P.; Blanc, F.; Talhi, C.; Franc, B.; Ganibal, C.; Wartelle, C.; Aguir, K. Increasing the sensitivity and selectivity of Metal Oxide gas sensors by controlling the sensitive layer polarization. In Proceedings of the 2012 IEEE Sensors, Taipei, Taiwan, 28–31 October 2012; pp. 1–4.
51. Ahlers, S.; Müller, G.; Doll, T. A rate equation approach to the gas sensitivity of thin film metal oxide materials. *Sens. Actuators B Chem.* **2005**, *107*, 587–599. [[CrossRef](#)]
52. Schipani, F.; Miller, D.R.; Ponce, M.A.; Aldao, C.M.; Akbar, S.A.; Morris, P.A. Electrical Characterization of Semiconductor Oxide-Based Gas Sensors Using Impedance Spectroscopy: A Review. *Rev. Adv. Sci. Eng.* **2016**, *5*, 86–105. [[CrossRef](#)]
53. Schipani, F.; Miller, D.; Ponce, M.; Aldao, C.; Akbar, S.; Morris, P.; Xu, J. Conduction mechanisms in SnO<sub>2</sub> single-nanowire gas sensors: An impedance spectroscopy study. *Sens. Actuators B Chem.* **2017**, *241*, 99–108. [[CrossRef](#)]
54. Szafraniak, B.; Kusior, A.; Radecka, M.; Zakrzewska, K. Impedance Spectroscopy in H<sub>2</sub> Sensing with TiO<sub>2</sub>/SnO<sub>2</sub> Nanomaterials. *Metrol. Meas. Syst.* **2020**, *27*, 417–425. [[CrossRef](#)]
55. Farva, U.; Kim, J. Growth temperature-dependent morphological, optical, and electrical study of SnO<sub>2</sub> thin film by atomic layer deposition. *Mater. Chem. Phys.* **2021**, *267*, 124584. [[CrossRef](#)]
56. Scragg, J.J.S.; Choubrac, L.; Lafond, A.; Ericson, T.; Platzer-Björkman, C. A low-temperature order-disorder transition in Cu<sub>2</sub>ZnSnS<sub>4</sub> thin films. *Appl. Phys. Lett.* **2014**, *104*, 041911. [[CrossRef](#)]
57. Fontané, X.; Izquierdo-Roca, V.; Saucedo, E.; Schorr, S.; Yukhymchuk, V.O.; Valakh, M.Y.; Pérez-Rodríguez, A.; Morante, J.R. Vibrational properties of stannite and kesterite type compounds: Raman scattering analysis of Cu<sub>2</sub>(Fe,Zn)SnS<sub>4</sub>. *J. Alloys Compd.* **2012**, *539*, 190–194. [[CrossRef](#)]
58. Guo, Y.; Wei, J.; Liu, Y.; Yang, T.; Xu, Z. Surfactant-Tuned Phase Structure and Morphologies of Cu<sub>2</sub>ZnSnS<sub>4</sub> Hierarchical Microstructures and Their Visible-Light Photocatalytic Activities. *Nanoscale Res. Lett.* **2017**, *12*, 181. [[CrossRef](#)] [[PubMed](#)]
59. Chenari, H.M.; Hassanzadeh, A.; Golzan, M.; Sedghi, H.; Talebian, M. Coulomb blockade phenomena and impedance spectroscopy studies in a double-barrier junction. *Solid State Commun.* **2010**, *150*, 2285–2287. [[CrossRef](#)]
60. Zhang, C.; Boudiba, A.; De Marco, P.; Snyders, R.; Olivier, M.-G.; Debliquy, M. Room temperature responses of visible-light illuminated WO<sub>3</sub> sensors to NO<sub>2</sub> in sub-ppm range. *Sens. Actuators B Chem.* **2013**, *181*, 395–401. [[CrossRef](#)]